
SPECTRAL PERSISTENT HOMOLOGY: PERSISTENCE SIGNALS

A PREPRINT

Michael E. Van Huffel
Department of Mathematics
ETH Zurich
Zurich, Switzerland
michavan@student.ethz.ch

Matteo Palo
Department of Mathematics
ETH Zurich
Zurich, Switzerland
mapalo@student.ethz.ch

December 29, 2023

ABSTRACT

In this paper, we present a novel family of descriptors for persistence diagrams, reconceptualizing them as signals in \mathbb{R}_+^2 . This marks a significant advancement in Topological Data Analysis. Our methodology transforms persistence diagrams into a finite-dimensional vector space through functionals of the discrete measures induced by these diagrams. While our focus is primarily on frequency-based transformations, we do not restrict our approach exclusively to this types of techniques. We term this family of transformations as *Persistence Signals* and prove stability for some members of this family against the 1-*Kantorovitch-Rubinstein* metric, ensuring its responsiveness to subtle data variations. Extensive comparative analysis reveals that our descriptor performs competitively with the current state-of-art from the topological data analysis literature, and often surpasses, the existing methods. This research not only introduces a groundbreaking perspective for data scientists but also establishes a foundation for future innovations in applying persistence diagrams in data analysis and machine learning.

Keywords Topological Data Analysis · Persistent Homology · Spectral Persistence · Frequency Transformations

1 Introduction

Topological Data Analysis (TDA) has emerged as a transformative approach in data science, providing unique insights into the underlying structure of complex datasets through the capture of their topological features. The effectiveness of machine learning algorithms, particularly in pattern recognition and feature extraction, underscores the importance of understanding data geometry. TDA offers a more sophisticated exploration of this geometric landscape, leading to numerous successful applications across various fields. Notable examples include neuroscience (Anderson et al. [2018], Dabaghian et al. [2012]), where TDA has also been instrumental in understanding complex neural networks and brain connectivity patterns. In the field of environmental science, TDA has been applied for climate data analysis, as seen in Nunez et al. [2019]. Additionally, TDA has made significant contributions to materials science, particularly in the study of the structure of materials, as exemplified by Donato et al. [2016]. These examples underscore the broad applicability and potential of TDA in enhancing our understanding of complex data across diverse scientific domains.

Persistent homology, a core methodology within TDA, systematically keeps track of the appearing and disappearing of topological characteristics across a sequence of nested topological spaces, a process documented in seminal works by Edelsbrunner and Harer [2008], and Zomorodian and Carlsson [2005]. These topological features are typically represented through persistence diagrams (PDs). However, the space of these diagrams is notably unstructured: they vary in the number of points they contain, and fundamental operations like addition and scalar multiplication are not clearly defined. This lack of structure, including the absence of a Hilbert space, as proved in Bubenik and Wagner [2020] and Mileyko et al. [2011], poses significant challenges in integrating persistence diagrams into machine learning workflows, where such a space is often crucial for diverse tools and techniques including classification, neural networks, and feature selection.

Our contribution in this study is multi-faceted and significant in the field of TDA. We introduce a novel family of descriptors, termed *Persistence Signals* (PS), which represent a paradigm shift in how persistence diagrams are interpreted and utilized. By reconceptualizing persistence diagrams as signals within the \mathbb{R}^2 space, we enable their transformation into a finite-dimensional vector space. This is achieved through the application of functionals to the discrete measures induced by these diagrams. Our methodology is not limited to frequency-based techniques, allowing for a broader scope of analysis and application. A key aspect of our contribution is the proof of stability of some member of the PS family against the 1-Kantorovich-Rubinstein metric. This crucial property underscores the robustness of our approach, ensuring that the PS descriptors are sensitive and responsive to subtle variations in data.

Our approach not only provides a novel method for vectorizing persistence diagrams but also bridges two crucial and burgeoning realms: TDA and signal processing theory. This fusion opens the doors to an entirely new perspective in data analysis, offering inspiring ways to unravel complex data patterns and extract meaningful insights. Our methodology stands as a testament to the synergy between these two fields, enabling a more intuitive and accessible approach to understanding and manipulating TDA structures. As such, we see this work as a pioneering step into a new domain of study that we call *Spectral Persistence Homology*. To the best of our knowledge, this is the first instance where tools from classical signal processing theory have been employed to achieve a nearly lossless information vectorization method. Our method requires minimal tuning and is designed to be user-friendly, making it accessible even to those with limited knowledge of TDA. This groundbreaking approach not only simplifies the application of TDA but also expands its potential to a wider audience, promising significant advancements in various fields that rely on complex data analysis.

The remainder of this paper is organized as follows: in Section 2, we review related work that connects TDA and ML, focusing particularly on classical methods of embedding persistence diagrams using vectorization or kernel methods. Section 3 delves into the background of persistent homology and persistent measures, offering foundational knowledge crucial for grasping the ideas from this work. In Section 4, we present our methodology along with the stability theorems that underpin it, providing theoretical insights into our approach. Section 5 is dedicated to showcasing our experimental results. Here, we not only present our findings but also compare them with standard methods from the TDA literature, highlighting the advancements our method brings. Finally, Section 6 is devoted to summarizing our key findings and outlining ideas for further work, suggesting potential avenues for future research and development based upon the groundwork established in this paper. The implementation of Persistence Signals has been made available to the public as an open-source resource¹.

2 Related Work

In the realm of TDA, efforts to reconcile statistics and machine learning have taken shape through two principal strategies. Initially, direct engagement with persistence diagrams involved exploring concepts such as the Fréchet mean Mileyko et al. [2011], confidence sets Perea et al. [2019], and metric learning methods employing distances like Wasserstein or bottleneck distances Fasy et al. [2014]. However, challenges arose due to the complex geometry inherent in persistence diagrams Wagner [2019].

To overcome these challenges, an alternative strategy seeks to map the space of persistence diagrams to more manageable alternatives where established machine learning algorithms can be applied. Two notable families have emerged:

Vectorization Methods. Among these methods, Persistence Images Adams et al. [2017], which partially inspired this work, are particularly notable. This approach first applies a Gaussian kernel function to the persistence diagram and then discretizes it over a grid. Another method for embedding persistence diagrams is the use of Persistence Landscapes Bubenik [2015], which represent the diagrams as landscapes of functions across various scales. Worth mentioning are their multi-parameter extensions, Carrière and Blumberg [2020], Vipond [2020], that enhance robustness using multi-parameter persistent homology.

More modern approaches include ATOL Royer et al. [2021], who utilizes a two-step process, computing a discrete measure supported on b points to approximate the average measure of the input data distribution and generating contrast functions to convert observed measures into b -dimensional vectors, and PersLay Carrière et al. [2020], that introduces a specialized neural network layer for vectorizing persistence diagrams.

Designing Specific Kernels. A second family of approaches involves crafting specific kernels on the space of persistence diagrams, such as the multi-scale kernel of Reininghaus et al. [2014], the weighted Gaussian kernel Kusano et al. [2016] and sliced Wasserstein kernel Carrière et al. [2017], all these methods captures topological features at different scales and often their performances are comparable to state-of-arts, albeit facing challenges in explicit representation and scalability.

¹<https://github.com/majkev/spectral-master>

3 Background

In this section we briefly provide an overview of persistent homology, along with its various output forms, specifically focusing on persistence diagrams and persistence measures.

3.1 Persistent Homology

Persistent homology, a cornerstone of TDA, offers a robust framework for analyzing the topological structure of datasets, such as point clouds or time-series. This methodology is adept at monitoring the evolution of homological features across various scales. For a comprehensive overview, readers are referred to Edelsbrunner and Morozov [2017]. The development of persistent homology has been significantly advanced by seminal contributions in the field, including the works of Zomorodian and Carlsson [2005], and Edelsbrunner et al. [2000]. The essence of persistent homology lies in its ability to effectively capture and track the changes in topological features across various scales. This is achieved through a filtration process, which involves a series of progressively inclusive topological spaces $X_0 \subseteq X_1 \subseteq \dots \subseteq X_n = X$, allowing for a detailed and granular analysis of the dataset's topological properties.

A standard approach for illustrating the insights obtained from persistent homology is the use of a persistence diagram. In our study, we adopt the notation for persistence diagrams as delineated in Monod [2022]. The detailed definition of persistence diagrams is provided in Definition 3.1.

Definition 3.1 A persistence diagram D is a locally finite multiset of points in the half-plane $\Omega = \{(x, y) \in \mathbb{R}^2 \mid x < y\}$ together with points on the diagonal $\partial\Omega = \{(x, x) \in \mathbb{R}^2\}$ counted with infinite multiplicity. Points in Ω are called off-diagonal points. We denote as persistence of a feature, the value $y - x$.

Remark 3.2 In this study, we operate under the assumption that all points on the diagram exhibit finite persistence.

The space of persistence diagrams can be endowed with a parametrized metric, denoted as d_s , where $1 \leq s \leq \infty$. This metric is known as the *Kantorovich-Rubinstein* distance, as detailed in Definition 3.3. For the sake of simplicity, we will henceforth refer to this metric as the *Wasserstein* distance.

Definition 3.3 Let $\|\cdot\|_q$ denote the q -norm on \mathbb{R}^2 for $1 \leq q \leq \infty$. Let D_1, D_2 be any two persistence diagrams. For $1 \leq p < \infty$, the p -Wasserstein distance is

$$W_{p,q}(D_1, D_2) = \inf_{\gamma} \left(\sum_{x \in D_1} \|x - \gamma(x)\|_q^p \right)^{\frac{1}{p}},$$

where γ ranges over all bijections between D_1 and D_2 .

Remark 3.4 If $p = q$ we denote $W_{p,p}$ as W_p for simplicity of notation.

Remark 3.5 For $p = \infty$, $W_{\infty,q}$ becomes the so called *bottleneck distance*.

The collection of all persistence diagrams that possess finite p -total persistence is represented by \mathcal{D}_p . As mentioned in Monod [2022], the metric space $(\mathcal{D}_p, W_{p,q})$ occupies a pivotal role in TDA. Particularly noteworthy is the case when $q = \infty$. In this scenario, the metric space $(\mathcal{D}_p, W_{p,\infty})$ constitutes a complete and separable metric space—essentially, a Polish space—for any $1 \leq p < \infty$. This characteristic endows the space with significant analytical power, as it ensures that statistical and probabilistic concepts such as probability measures, expectations, and variances are well-defined within this context, as elucidated by Mileyko et al. [2011].

3.2 Persistence Measures

In Chazal et al. [2013], an alternative perspective is presented, suggesting the definition of a persistence diagram as a measure expressed by $\mu = \sum_{\mathbf{x} \in D} m(\mathbf{x})\delta_{\mathbf{x}}$, where $D \subset \Omega$ is locally finite, and $m(\mathbf{x}) \in \mathbb{N}$ is the multiplicity of each \mathbf{x} , for all $\mathbf{x} \in D$. This results in μ being a locally finite measure supported on Ω with an integer mass on each point of its support. This perspective encourages the consideration of more general Radon measures supported on the upper half-plane Ω , Chazal et al. [2013]. By incorporating such measures, a statistical viewpoint can be introduced into the realm of persistent homology.

Expanding upon the aforementioned measure-centric perspective, in Divol and Lacombe [2019], the authors propose metrics applicable to the space \mathcal{M} of Radon measures with support on Ω . Specifically, for finite values of $p \geq 1$,

the authors articulate the definition of *persistence* for a measure $\mu \in \mathcal{M}$ as $\text{Pers}_p(\mu) := \int_{\Omega} d(x, \partial\Omega)^p d\mu(x)$. Here, the term $d(x, \partial\Omega) := \inf_{y \in \partial\Omega} d(x, y)$ signifies the distance from a point $x \in \Omega$ to its orthogonal projection onto the diagonal $\partial\Omega$. Furthermore, the authors establish the set \mathcal{M}^p as the collection encompassing all persistence measures with finite p .

In the realm of persistence measures, the concept of the optimal partial transport distance plays a pivotal role. This distance has been formally introduced by Figalli and Gigli [2010] and is detailed in Definition 3.6. In our study, we use the same notation as in Monod [2022].

Definition 3.6 *Given two persistence measures μ and ν , their optimal partial transport distance is defined as*

$$\text{OT}_{p,q}(\mu, \nu) = \left(\inf_{\pi} \int_{\bar{\Omega} \times \bar{\Omega}} \|x - y\|_q^p d\Pi(x, y) \right)^{1/p},$$

where $\bar{\Omega} = \Omega \cup \partial\Omega$, and Π is a Radon measure on $\bar{\Omega} \times \bar{\Omega}$ that satisfies $\Pi(P \times \bar{\Omega}) = \mu(P)$ and $\Pi(\bar{\Omega} \times Q) = \nu(Q)$ for all Borel sets $P, Q \subseteq \Omega$.

Remark 3.7 *For the case where $p = q$, we simplify the notation to OT_p .*

Building on this foundational concept, we can then consider the metric space defined as $(\mathcal{M}^p, \text{OT}_p)$. Here, \mathcal{M}^p is equipped with the optimal partial transport distance OT_p , serving as its metric. As established in Divol and Lacombe [2019], the subset \mathcal{D}^p within \mathcal{M}^p maintains its closed subspace property and inherits the key characteristics of \mathcal{M}^p . This includes being a Polish space, applicable for all $1 \leq p < \infty$ and $1 \leq q \leq \infty$. Consequently, the space $(\mathcal{M}_p, \text{OT}_{p,q})$ emerges as a robust framework for statistical and probabilistic applications. Moreover, within this framework, $\text{OT}_{p,q}$ coincide with $W_{p,q}$ when restricted to \mathcal{D}_p . As also mentioned in Monod [2022], this alignment underscores the role of persistence measures and the optimal partial transport distance as comprehensive extensions to traditional persistence diagrams and the p -Wasserstein distance.

4 Methodology

In this section, we introduce the *Spectral Persistent Homology* framework for embedding persistence measures in vector spaces along with the stability results.

As an overview, the process of vectorizing a persistence diagram using *Persistence Signals*, depicted in Algorithm 4, involves two distinct steps: first, we compute the *discretized persistence diagram* (refer to Section 4.2), transforming the persistence diagram into a format suitable for further processing. Following this, a functional is applied to this discretized representation to achieve an embedding within a vector space. As detailed in Section 4.1, this work primarily focuses on functionals that define valid frequency and time-frequency distribution functions. Notably, these include the Fourier Transform for frequency distribution, and the Wavelet and Gabor Transforms for time-frequency distribution. These transforms will be introduced in the subsequent subsection. It's important to note, however, that our framework is versatile and not exclusively limited to these transforms.

Algorithm 1 Persistence Signals vectorization

Require: f : Transformation function with hyperparameters, Grid size: $\{N, M\}$, PDs	▷ Section 4.1
1: Discretize PDs on grid	▷ Section 4.2
2: Compute Functional on grid	▷ Section 4.1.1
Ensure: Embedding of PDs	

4.1 Functionals on Persistence Measures

Given $\mu \in \mathcal{M}^p$, we consider a functional Ψ defined by

$$\Psi(\mu)(f) := \Psi_{\mu}(f) = \int_{\Omega} f(\mathbf{x}, \cdot) d\mu(\mathbf{x}).$$

This functional represents a mapping from the measure space \mathcal{M}^p to a space of functions $\mathcal{F}(\mathcal{M}^p)$. In our case, since the measure μ is discrete and is a measure induced by a persistence diagram D , have that

$$\Psi_{\mu}(f) = \sum_{\mathbf{x} \in D} m(\mathbf{x}) f(\mathbf{x}, \cdot).$$

In this paper, we concentrate on functionals that establish valid frequency and time-frequency distribution functions (hereinafter referred to, for simplicity, as *frequency transforms*). Both families of these transforms are mapped onto the complex hyperplane (*frequency domain* from now on). Consequently, $\mathcal{F}(\mathcal{M}^p)$ can be characterized as a vector space. The choice of selecting functionals that map into the frequency domain is motivated by the fact that persistent diagrams summarize topological features across various length scales of a filtration parameter. This parameter can be seen as a *timestamp*, indicating when topological features emerge or vanish, therefore it seems natural to interpret them as signals.

In this work, we focus on three possible choices of f : two time-frequency distributions, namely the Gabor Transform and the Wavelet Transform, and one frequency transform, specifically the Fourier Transform (which can be regarded as a special case of the Gabor Transform).

Fourier Transform. Let $f(\mathbf{x}, \omega) = e^{-2\pi j \omega^\top \mathbf{x}}$. We have that $\Psi_{\mu, F}(\omega) : \mathcal{M}^p \mapsto \mathbb{C}$ represents the Fourier Transform of the measure μ . This choice is motivated by the Fourier Transform's ability to decompose signals into their constituent frequencies, providing a global frequency perspective that is essential in understanding the overall structure of persistence diagrams.

Wavelets Transform. Let $f(\mathbf{x}, a, \mathbf{b}) = \frac{1}{a} \phi_{a, \mathbf{b}}(\mathbf{x})$, where $\phi_{a, \mathbf{b}}$ is an orthonormal wavelet, a is a scalar representing the scale factor, and \mathbf{b} is a 2D vector representing the translation. Then it holds that $\Psi_{\mu, \mathcal{W}}(a, \mathbf{b}) : \mathcal{M}^p \rightarrow \mathbb{C}$ represents the Wavelet Transform of the measure μ . Chosen for its spatial-frequency localization, the Wavelet Transform has the ability to adjust focus between fine and broad details aligning well with the varying scales inherent in topological data.

Gabor Transform. Let $f(\mathbf{t}, \mathbf{x}, \lambda, \theta, \psi, \sigma, \gamma) = g_{\lambda, \theta, \psi, \sigma, \gamma}(t_1 - x_1, t_2 - x_2)$, where $g_{\lambda, \theta, \psi, \sigma, \gamma}(x, y)$ is the Gabor kernel defined as:

$$g_{\lambda, \theta, \psi, \sigma, \gamma}(x, y) = \exp\left(-\frac{x'^2 + \gamma^2 y'^2}{2\sigma^2}\right) \cdot \exp\left(j\left(2\pi \frac{x'}{\lambda} + \psi\right)\right),$$

with $x' = x \cos \theta + y \sin \theta$ and $y' = -x \sin \theta + y \cos \theta$. Here, $\lambda \geq 0$ is the wavelength of the sinusoidal factor, $\theta \in [0, 2\pi]$ is the orientation of the normal to the parallel stripes of a Gabor function, $\psi \in [0, 2\pi]$ is the phase offset, $\sigma \geq 0$ is the standard deviation of the Gaussian envelope, and $\gamma \in [0, 1]$ is the spatial aspect ratio. We have that $\Psi_{\mu, \mathcal{G}}(\mathbf{t}, \lambda, \theta, \psi, \sigma, \gamma) : \mathcal{M}^p \rightarrow \mathbb{C}$ represents the Gabor Transform of the measure μ . The Gabor Transform, combining both time and frequency information, provides a localized frequency analysis of the signals arising from the persistence diagrams. This transform is utilized for its proficiency in localized time-frequency analysis, essential for understanding the dynamic evolution of topological features in persistence diagrams. In our setup, we take $\theta = 0$, $\psi \in \{0, \pi/2\}$ and omit it from the parameters from now on.

4.1.1 Grid Based Approach in Computational Persistence Theory

Considering the practical computational requirements of all transforms under consideration, our theory is formulated based on the computation of *discretized persistence diagrams* (for details, refer to Section 4.2). In this framework, measures are confined to allocating mass exclusively at points on a grid (for a definition of the grid measure subspace Γ_p , refer to Lemma 4.1). Consequently, to compute the embedding, we employ a *discretized* version of the transforms discussed in the previous section. For a comprehensive literature review on the Discrete Fourier Transform (DFT), Discrete Wavelet Transform (DWT), and Discrete Gabor Transform (DGT), we direct the reader to Oppenheim and Schaffer [2009] and Søndergaard [2007]. Given a persistence measure $\mu \in \Gamma_p$, the three functionals on the transforms depicted in Section 4.1 are now formulated as follows:

Discrete Fourier Functional. $\Psi_{\mu, F}(x_i, x_j) = \sum_{x_m, x_n \in G_{N, M}} m(x_m, x_n) e^{-2\pi j \left(\frac{x_m}{x_M} \cdot x_i + \frac{x_n}{x_N} \cdot x_j\right)}$. This functional is computed using the widely known Fast Fourier Transform (FFT) algorithm, Cooley and Tukey [1965]. The magnitude and phase of the FFT output are extracted, flattened, and concatenated to form the FFT vectorization.

Discrete Wavelets Functional. $\Psi_{\mu, \mathcal{W}}(a, \mathbf{b}, x_i, x_j) = \sum_{x_m, x_n \in G_{N, M}} m(x_m, x_n) \cdot \phi_{a, \mathbf{b}}(x_i - x_m, x_j - x_n)$. This functional is computed for standard orthonormal wavelets (Haar, Coiflet, Daubechies, . . .) using Fast Wavelet Transform (FWT) algorithm, Shensa [1992]. Coefficients of FWT are then extracted, concatenated and used as vectorization.

Discrete Gabor Functional. $\Psi_{\mu, \mathcal{G}}(\lambda, \psi, \sigma, \gamma, \mathcal{N}_G(\cdot), x_i, x_j) = \sum_{x_m, x_n \in \mathcal{N}_G(x_i, x_j)} m(x_m, x_n) \cdot g_{\lambda, \psi, \sigma, \gamma}(x_i - x_m, x_j - x_n)$. In the above formula, $\mathcal{N}_G(x_i, x_j)$ represents the neighborhood grid around the point (x_i, x_j) . This neighborhood is used to limit the computation to a local region around each point, enhancing efficiency and focusing on local features. The DGT employs convolution algorithms for computation. To achieve vectorization of the DGT, both the magnitude and phase of the DGT output are extracted. These components are then flattened and concatenated, forming the comprehensive DGT embedding.

4.2 Discretized Persistence Diagrams

The concept of *discretization of persistence diagrams* naturally arises from the grid-based algorithms used in real-life computations of the transforms outlined in Section 4.1, and it forms a critical aspect of our methodology.

This discretization process in our methodology involves two primary steps.

4.2.1 Shifting Step

Taking inspiration from the work by Adams et al. [2017], we first apply a shifting process to the measure induced by a persistence diagram using shift τ . Specifically, let $\mu \in \mathcal{M}^p$ represent a persistence measure in birth-death coordinates. We define $\tau : \mathcal{M}^p \rightarrow \mathcal{M}^p$ as a linear shifting operation $\tau(\mu) = (x_1, x_2 - x_1)$. Upon applying this shift, we obtain $\tau(\mu)$, the transformed measure now represented in birth-persistence coordinates in the space $\tilde{\Omega}$. This shifting is applied with the intention of better aligning the shifted diagram with the subsequent step of discretization on a grid. The motivation for this shifting lies in the distribution of points in the persistence diagram. Initially, in birth-death coordinates, points are located along the upper diagonal $\partial\Omega$, leaving the bottom diagonal empty. This distribution can be suboptimal for certain analyses, especially when considering a square grid for discretization aligned with the axis. The shift to birth-persistence coordinates changes this, as the points no longer lie solely on the upper diagonal. Instead, this shifting process redistributes the points more uniformly across the grid, making better use of the available space.

4.2.2 Mapping Step

Lemma 4.1 *Let $G_{N,M}$ be a regular grid on \mathbb{R}_+^2 consisting of points $\{(x_i, y_j) \mid x_i = i\Delta, y_j = j\Delta, i = 0, \dots, N-1, j = 0, \dots, M-1\}$ where Δ is the grid finesse. Define \mathcal{S} as the σ -algebra containing all subsets of $G_{N,M}$, and $\mu : \mathcal{S} \rightarrow [0, \infty]$ as a measure such that for any $A \in \mathcal{S}$, $\mu(A) = \sum_{(x_i, y_j) \in A} m_{ij} \in \mathcal{M}^p$ where m_{ij} is a integer mass assigned to the point (x_i, y_j) . The triple $\Gamma_p = (G_{N,M}, \mathcal{S}, \mu)$ constitutes a discrete measure space.*

The proof of Lemma 4.1 is straightforward and follows directly from the axioms defining a measure space.

Proposition 4.2 *Let $\Gamma_p \subset \mathcal{M}^p$ be a discrete measure space as defined in Lemma 4.1. For a persistence diagram D and a measure $\mu = \sum_{\mathbf{x} \in \tau(D)} m(\mathbf{x})\delta_{\mathbf{x}} \in \mathcal{M}^p$, consider the 1-Optimal partial transport distance (1-OT) between μ and any measure $\nu \in \Gamma_p$. Consider the optimization problem*

$$\nu^* = \arg \min_{\nu' \in \Gamma_p} OT_1(\mu, \nu'), \quad \text{s.t.} \quad \nu'(G_{N,M}) = \mu(D).$$

If we choose $\nu = \sum_{\mathbf{x} \in \tau(D)} m(\Theta(\mathbf{x}))\delta_{\Theta(\mathbf{x})}$, where $\Theta : \mathbb{R}_+^2 \rightarrow G_{N,M}$ is a mapping that assigns each point $\mathbf{x} \in \tau(D)$ to the closest point in $G_{N,M}$ minimizing $\|\mathbf{x} - \mathbf{x}'\|_1$, then it holds that $\nu = \nu^$ is the solution to the optimization problem.*

The proof of Proposition 4.2 is provided in Appendix A.1.

By Proposition 4.2, we therefore obtain a persistence measure ν^* on Γ_p . We refer to ν^* as the measure induced by the so-called *discretized persistence diagram*.

4.3 Stability

Given the inevitable presence of noise or measurement errors, it is essential for data analysis tools to be stable against minor input perturbations.

In line with this, we have established stability results with respect to the 1-Wasserstein metric for two of the transforms we considered, namely the Fourier and Gabor Transforms. For the Wavelet Transform, there does not always exist a closed-form expression, which makes finding stability results very challenging. Extending these results to the Wavelet Transform remains a challenge for future work.

Theorem 4.3 *Let $\mu = \sum_{\mathbf{x} \in \Theta_\tau(D)} \delta_{\mathbf{x}}$ and $\nu = \sum_{\mathbf{x} \in \Theta_\tau(D')} \delta_{\mathbf{x}}$ be two measures on the discretized persistence diagrams of D, D' , let f be a functional, either Gabor or Fourier (refer to Section 4.1). Then, there exists a finite constant c such that:*

$$\|\Psi_\mu(f) - \Psi_\nu(f)\|_\infty \leq c \cdot W_1(D, D').$$

This statement proposes a bound on the difference between the functionals of the two measures, scaled by a constant and the 1-Wasserstein distance between the original persistence diagrams.

Remark 4.4 *The following expressions are equivalent:*

$$\mu = \sum_{\mathbf{x} \in \Theta(\tau(D))} m(\mathbf{x})\delta_{\mathbf{x}} = \sum_{\mathbf{x} \in \Theta_{\tau}(D)} \delta_{\mathbf{x}}.$$

For convenience, we used the latter and cleaner notation in Theorem 4.3, where the multiplicity of each point is implicitly accounted for within the summation. For example, if a point appears with a multiplicity of 2, it is effectively included twice in the summation.

The proof of Theorem 4.3 is provided in Appendix A.2.

5 Results

In this section, we demonstrate how PS effectively preserve topological information, proving to be as competitive as state-of-the-art methods from the TDA literature. Our experiments are conducted on two types of classification tasks: graph-based classification and classification of point clouds derived from dynamical systems. In our experiments, we utilized a Vanilla Random Forest classifier from `scikit-learn`. The choice of a random forest classifier was driven by two primary considerations: Firstly, it facilitates a direct comparison with the study conducted by Royer et al. [2021]. Secondly, in line with our objective to showcase the overall effectiveness of our methods relative to existing literature, employing this type of classifier helps to circumvent the necessity for elaborate infrastructure or extensive fine-tuning. Such an approach ensures that the results are not excessively influenced by particular design choices.

5.1 Graph Classification

Given the growing interest in graph data within learning problems, the standard graph classification framework, denoted as $\Omega := (G, y)$, represents a finite collection of graphs and their corresponding labels in $\mathcal{G} \times \mathcal{Y}$.

Definition 5.1 *For a graph $\mathcal{G} = (V, E)$, the HKS function with diffusion parameter t is defined for each vertex $v \in V$ as*

$$HKS_t(v) = \sum_{k=1}^{|V|} \exp(-t\lambda_k) \psi_k(v)^2,$$

where λ_k is the k -th eigenvalue of the normalized graph Laplacian, and ψ_k is the corresponding eigenfunction.

A significant advancement in TDA for graph classification is attributed to the work in Carriere et al. [2020], which introduced a method for extracting topological information from graphs using heat kernel signatures (HKS), as detailed in Definition 5.1 and further explored in Hu et al. [2014]. This approach involves extended persistence, encoding the topological structure of graphs and resulting in four types of finite persistence topological features.

These extended persistence diagrams not only offer richer information than conventional ones but also ensure data points have finite coordinates, enhancing their utility and reliability.

In our study, we benchmarked our methods against a variety of graph datasets that are widely recognized as standard benchmarks in graph classification research. The datasets include IMDB-B and IMDB-M, which consist of social graphs and are sourced from Tran et al. [2018], as well as COX2, DHFR, MUTAG, and PROTEINS. These latter datasets, also obtained from Tran et al. [2018], are derived from chemoinformatics and bioinformatics fields.

We adopt the methodology from Royer et al. [2021] for generating extended persistence diagrams, using two specific HKS diffusion times ($t_1 = .1$ and $t_2 = 10$), focusing solely on the topological structure without considering additional graph attributes. For the evaluation, we used three distinct square grid sizes— 20×20 , 32×32 , and 50×50 —across all our proposed transforms when dealing with both Biomedical and Social Networking graph problems.

Regarding the Wavelet Transform, we experimented with six different wavelet types: Daubechies (dbN) and Coiflet ($coifN$) wavelets for $N = 1, 2, 3$. For the Gabor Transform, we implemented it with a kernel size that is half of the grid size and set the parameters to $\sigma = 5, \theta = 0, \lambda = 10, \gamma = 0.5, \psi = 0$. This setup effectively utilizes only the *real* part of the output (since $\psi = 0$). It is important to note that these parameters were not individually fine-tuned for each task in this pre-print, but rather were used as *default* settings. We refer to this specific configuration as the *Real Vanilla Gabor Transform*.

The highest accuracies achieved with these transforms are presented in Table 5.1. Detailed observations for each transform across the different grids can be found in the Appendix B. Performance is assessed through 10-fold evaluations on each dataset, reporting both average and best 10-fold results.

Dataset	SV [†]	RetGK [*]	FGSD [†]	GCNN [†]	GIN [†]	P [†]	MP [†]	Perslay [*]	ATOL [*]	BBA [†]	PS	
											Mean [*]	Max [†]
MUTAG	88.3	90.3	92.1	86.7	89.0	79.2	86.1	89.8	88.3	90.4	89.8	91.7
COX2	78.4	81.4	-	-	-	76.0	79.9	80.9	79.4	81.2	80.6	82.4
PROTEINS	72.6	75.8	73.4	76.3	75.8	65.4	67.5	74.8	71.4	74.7	72.8	73.6
DHFR	78.4	81.5	-	-	-	70.9	81.7	80.3	82.7	80.5	81.8	83.1
IMDB-B	72.9	71.9	73.6	73.1	74.3	54.0	68.7	71.2	74.8	69.4	68.4	69.8
IMDB-M	50.3	47.7	52.4	50.3	52.1	36.3	46.9	48.8	47.8	46.7	43.7	44.4

Table 1: Comparative Analysis of Classification Accuracy on Benchmark Graph Datasets. Note: The symbol [†] indicates that the performance should be compared with the *Max* metric, while the symbol ^{*} denotes that the comparison should be made with the *Mean* metric.

All computations were conducted on a single laptop, an Apple M3 Pro equipped with an 11-core CPU.

In line with Carriere et al. [2020], Royer et al. [2021], and Hacquard [2023], we benchmark our performance against the leading methods for these problems, as well as against traditional topological methods documented in the literature. For the latter, P signifies the superior method between the Persistence Images and Persistence Landscapes, while MP indicates the best between Multiparameter Persistence Images and Landscape. All these persistence-based vectorizations are coupled with a Vanilla XGBoost classifier for the learning task. In contrast, the top performing methods for these graph problems predominantly utilize graph kernel methods specifically designed for graph problems. These include: a scale-variant topological method (SV from Tran et al. [2018]), a graph kernel method based on random walks (RetGK from Zhang et al. [2018]), a graph embedding method using spectral distances (FGSD from Verma and Zhang [2017]), a Capsule Graph Neural Network (GCNN from Zhang and Chen [2019]), and a Graph Isomorphism Network (GIN from Xu et al. [2019]). Additionally, we also compare our results with those of PersLay (from Carriere et al. [2020]), a neural network-driven topological vectorization method encapsulating most topological frameworks in the literature, and ATOL (from Royer et al. [2021]), which introduces a fast, learned, unsupervised vectorization method for measures in Euclidean spaces. Lastly, we compare with BBA from Hacquard [2023], which employs rectangle-based classification with boosting on persistence measures. Notably, both PersLay and ATOL use the same eight diagrams with HKS parameters as ours. However, in a few cases for PersLay, the authors employed two HKS diffusion times and then discarded one of them, without any loss in performance.

The accuracy of competitors, as reported in their respective publications (except for P and MP, which are cited from Hacquard [2023]), should be interpreted as follows: For RetGK, ATOL, and PersLay, the evaluation procedure was carried out over ten 10-fold validations, similar to our approach, making the results directly comparable to our *Mean* in Table 5.1. For FGSD, SV, GIN, GCNN, BBA, P, and MP, the average accuracy was calculated using a single 10-fold validation; therefore, their performance should be compared with our *Max* (maintaining consistency with Carriere et al. [2020]).

In Table 5.1, our results are at the state-of-the-art for the Biomedical benchmark datasets. Our methods consistently surpass all traditional TDA methods, such as P and MP and moreover prove parallel or sometimes better performance in some task with more advanced technique such as ATOL, PersLay, SV and BBA.

Significantly, on the MUTAG dataset, our method outperforms all comparable techniques, achieving the same mean accuracy as Perslay but with a superior maximum accuracy².

Moreover, our performance on the COX2 and DHFR datasets is particularly noteworthy, with our methods achieving the second-highest average accuracy in both instances. Specifically for topological methods, our approach attains the highest maximum accuracy on the DHFR dataset.

It is important to note, however, that a direct comparison of our results with Perslay’s findings for the IMDB and PROTEINS datasets is not feasible, owing to Perslay’s unique preprocessing approach that focuses exclusively on the 500 points furthest from the diagonal.

Although our methods demonstrate exceptional performance overall, it should be acknowledged that for the Social Networking datasets, they are slightly below the current best methods.

5.2 Dynamical systems (Orbit5K Dataset)

The Orbit5K dataset, a commonly used benchmark in TDA for classification methods and for modeling DNA microarray flows, is characterized by chaotic trajectories within the unit cube $[0, 1]^2$, exhibiting unique topological

²The maximum accuracies of Perslay are not included in Table 5.1; for these details, please refer to Carriere et al. [2020].

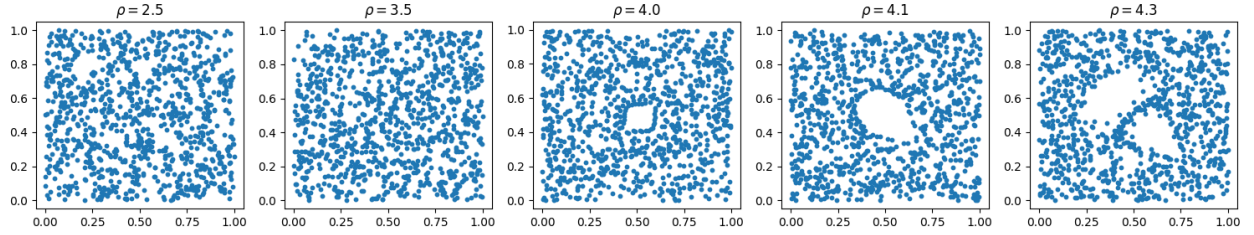


Figure 1: Representative Point Cloud Samples from the Orbit5K Dataset.

features dependent on a parameter $\rho > 0$. Notably, this dataset is the same as referenced in various studies Adams et al. [2017], Le and Yamada [2018], Carrière et al. [2017], Hacquard [2023], Carriere et al. [2020], Royer et al. [2021]. For each ρ class, we form point clouds by iterating the following recursive equations for a sequence of 1000 points, beginning from a random initial point (x_0, y_0) in $[0, 1]^2$:

$$\begin{aligned} x_{n+1} &= x_n + \rho y_n(1 - y_n) \pmod{1}, \\ y_{n+1} &= y_n + \rho x_{n+1}(1 - x_{n+1}) \pmod{1}. \end{aligned}$$

Figure 1 displays one sample per class, illustrating the diversity and challenge involved in this classification task.

We generated 700 training and 300 testing datasets for each ρ class, conducting a one-versus-one classification and using persistence diagrams for both H_1 and H_0 homologies, following the approach described in Le and Yamada [2018]. We employ the same transforms with hyperparameter settings as described in the previous subsection. We adopt a regular square grid of 64×64 and 128×128 for all transforms in this learning task. The highest accuracies achieved with our transforms are presented in Table 5.2. Detailed observations for each transform across the different grids are available in Appendix B. For this dynamical particles classification task, we report the accuracy averaged over 10 runs.

In line with Carriere et al. [2020] and Hacquard [2023], we compare our methods with four kernel methods on persistence diagrams: Persistence Scale Space Kernel (PSS-K from Reininghaus et al. [2015]), Persistence Weighted Gaussian Kernel (PWG-K from Kusano et al. [2016]), Sliced Wasserstein Kernel (SW-K from Carrière et al. [2017]), and Persistence Fisher Kernel (PF-K from Le and Yamada [2018]). Moreover, we compare with two neural network architectures, Perslay and Persformer (respectively from Carriere et al. [2020] and Reinauer et al. [2021]), Persistence Images (PI from Adams et al. [2017]), and a rectangle-based classification algorithm on persistence measures (BBA from Hacquard [2023]). The accuracies in Table 5.2 for our competitor methods are sourced from Le and Yamada [2018] for the kernel-based approaches, and from the respective original publications for the non-kernel methods. Our methods outperform most of the kernel methods, Persistence Images, and BBA classification, but are slightly less effective than the neural networks.

PSS-K [†]	PWG-K [†]	SW-K [†]	PF-K [†]	PI*	Perslay [†]	Persformer*	BBA*	PS*
72.38(±2.4)	76.63(±.7)	83.6(±.9)	85.9(±.8)	82.5	87.7(±1.0)	91.2(±.8)	83.3(±.5)	84.6(±.8)

Table 2: Comparative Classification Accuracy on the Orbit5K Dataset. Notes: [†] denotes methods with accuracy averaged over 100 runs; * indicates averaging over 10 runs; * signifies an average over 5 runs. For Persistence Images, no standard deviation is reported in Adams et al. [2017].

6 Conclusion and further work

In this study, we introduced a new vectorization framework for persistence diagrams by treating them as signals on \mathbb{R}_+^2 . We employed a functional-based transforms, focusing particularly on frequency methods. This approach has proven to be stable and effective in embedding information into a vector space, preserving key topological features. Its performance, either comparable or superior to leading methods, is demonstrated across various graph classification tasks and synthetic dynamical particle classifications. The simplicity of our method, along with its potential for enhancement, makes it a strong contender in the field of TDA vectorization techniques.

However, our approach is not without limitations. A significant challenge lies in the choice of grid. Presently, the grid’s fine granularity entails high computational expense for subsequent use of our vectorization in classical ML pipelines

due to high dimensionality of the embedding. Analysis of various persistence diagrams reveals a concentration of points near the origin, contrasting with extended areas of low point density. Consequently, many grid points remain unassociated with any persistence diagram points, resulting in numerous zeros in integral transforms. These zeros contribute little to no information gain, serving primarily to inflate the dimensionality of the embedding.

To address this, a non-uniform, adaptive grid that aligns with the distribution of points in persistence diagrams appears to be a more efficient alternative.

Furthermore, our methodology is not confined to the frequency domain. Future research could explore other domains, aiming to identify additional functionals that effectively retain the information within persistence diagrams.

Another prospective direction for future work involves incorporating our vectorization concept into frameworks akin to those described in Carriere et al. [2020] or Reinauer et al. [2021]. This integration could leverage neural networks or transformer architectures to refine the dimensionality of our embeddings, potentially enhancing both performance and applicability.

References

- Keri L. Anderson, Jeffrey S. Anderson, Sourabh Palande, and Bei Wang. Topological data analysis of functional mri connectivity in time and space domains. *Connectomics in neuroImaging : second international workshop, CNI 2018, held in conjunction with MICCAI 2018, Granada, Spain, September 20, 2018 : proceedings. CNI (Workshop)*, 11083: 67–77, 2018. URL <https://api.semanticscholar.org/CorpusID:52287547>.
- Yuri Dabaghian, Facundo Mémoli, Loren Frank, and Gunnar Carlsson. A topological paradigm for hippocampal spatial map formation using persistent homology. *PLoS Computational Biology*, 8(8):e1002581, 2012. doi:10.1371/journal.pcbi.1002581. URL <https://doi.org/10.1371/journal.pcbi.1002581>. Epub 2012 Aug 9.
- A. Nunez et al. Climate networks based on phase synchronization analysis track el-niño. *Progress of Theoretical and Experimental Physics*, 2019(8):083I01, 2019. doi:10.1093/ptep/ptz082. URL <https://academic.oup.com/ptps/article/doi/10.1143/PTPS.179.178/1915732>.
- Irene Donato, Matteo Gori, Marco Pettini, Giovanni Petri, Sarah De Nigris, Roberto Franzosi, and Francesco Vaccarino. Persistent homology analysis of phase transitions. *Physical Review E*, 93(5):052138, 2016. doi:10.1103/PhysRevE.93.052138. URL <https://link.aps.org/doi/10.1103/PhysRevE.93.052138>.
- Herbert Edelsbrunner and John Harer. Persistent homology - a survey. *Contemporary Mathematics*, 453:257–282, 2008.
- Afra Zomorodian and Gunnar Carlsson. Computing persistent homology. *Discrete and Computational Geometry*, 33(2):249–274, 2005. doi:10.1007/s00454-004-1146-y. URL <https://www.mendeley.com/catalogue/337da92b-4e42-38b2-b353-1bfa55eb1b69/>.
- Peter Bubenik and Alexander Wagner. Embeddings of persistence diagrams into hilbert spaces. *Journal of Applied and Computational Topology*, 4(3):353–385, 2020. doi:10.1007/s41468-020-00056-w. URL <https://link.springer.com/article/10.1007/s41468-020-00056-w>.
- Yuriy Mileyko, Sayan Mukherjee, and John Harer. Probability measures on the space of persistence diagrams. *Inverse Problems*, 27(12):124007, nov 2011. doi:10.1088/0266-5611/27/12/124007. URL <https://dx.doi.org/10.1088/0266-5611/27/12/124007>.
- Jose A. Perea, Elizabeth Munch, and Firas A. Khasawneh. Approximating continuous functions on persistence diagrams using template functions. *arXiv preprint arXiv:1902.07190*, 2019.
- Brittany Terese Fasy, Fabrizio Lecci, Alessandro Rinaldo, Larry Wasserman, Sivaraman Balakrishnan, and Aarti Singh. Confidence sets for persistence diagrams. *Annals of Statistics*, 42(6):2301–2339, 2014.
- Hubert Wagner. Nonembeddability of persistence diagrams with $p > 2$ wasserstein metric. *arXiv preprint arXiv:1910.13935*, 2019.
- Henry Adams, Tegan Emerson, Michael Kirby, Rachel Neville, Chris Peterson, Patrick Shipman, Sofya Chepushtanova, Eric Hanson, Francis Motta, and Lori Ziegelmeier. Persistence images: a stable vector representation of persistent homology. *Journal of Machine Learning Research*, 18(8):1–35, 2017.
- Peter Bubenik. Statistical topological data analysis using persistence landscapes. *Journal of Machine Learning Research*, 16(3):77–102, 2015.
- Mathieu Carrière and Andrew Blumberg. Multiparameter persistence image for topological machine learning. In H. Larochelle, M. Ranzato, R. Hadsell, M.F. Balcan, and H. Lin, editors, *Advances in Neural Information Processing*

- Systems*, volume 33, pages 22432–22444. Curran Associates, Inc., 2020. URL https://proceedings.neurips.cc/paper_files/paper/2020/file/fdff71fcab656abfbefaabecab1a7f6d-Paper.pdf.
- Oliver Vipond. Multiparameter persistence landscapes. *Journal of Machine Learning Research*, 21(61):1–38, 2020. URL <http://jmlr.org/papers/v21/19-054.html>.
- Martin Royer, Frederic Chazal, Clément Levrard, Yuhei Umeda, and Yuichi Ike. Atol: Measure vectorization for automatic topologically-oriented learning. In Arindam Banerjee and Kenji Fukumizu, editors, *Proceedings of The 24th International Conference on Artificial Intelligence and Statistics*, volume 130 of *Proceedings of Machine Learning Research*, pages 1000–1008. PMLR, 13–15 Apr 2021. URL <https://proceedings.mlr.press/v130/royer21a.html>.
- Mathieu Carriere, Frederic Chazal, Yuichi Ike, Theo Lacombe, Martin Royer, and Yuhei Umeda. Perslay: A neural network layer for persistence diagrams and new graph topological signatures. In Silvia Chiappa and Roberto Calandra, editors, *Proceedings of the Twenty Third International Conference on Artificial Intelligence and Statistics*, volume 108 of *Proceedings of Machine Learning Research*, pages 2786–2796. PMLR, 26–28 Aug 2020. URL <https://proceedings.mlr.press/v108/carriere20a.html>.
- Jan Reininghaus, Stefan Huber, Ulrich Bauer, and Roland Kwitt. A stable multi-scale kernel for topological machine learning, 2014.
- Genki Kusano, Yasuaki Hiraoka, and Kenji Fukumizu. Persistence weighted gaussian kernel for topological data analysis. In *International Conference on Machine Learning*, volume 48, pages 2004–2013, Jun 2016.
- Mathieu Carrière, Marco Cuturi, and Steve Oudot. Sliced wasserstein kernel for persistence diagrams. In *International Conference on Machine Learning*, volume 70, pages 664–673, Jul 2017.
- H. Edelsbrunner and D. Morozov. *Persistent Homology*. CRC Press, 3 edition, 2017. To appear.
- H. Edelsbrunner, D. Letscher, and A. Zomorodian. Topological persistence and simplification. In *Proceedings 41st Annual Symposium on Foundations of Computer Science*, pages 454–463, 2000.
- Yueqi Monod. Approximating persistent homology for large datasets. *arXiv preprint arXiv:2204.09155*, 2022.
- Frédéric Chazal, Vin de Silva, Marc Glisse, and Steve Oudot. The structure and stability of persistence modules. *arXiv preprint arXiv:1207.3674*, Mar 2013.
- Vincent Divol and Théo Lacombe. Understanding the topology and the geometry of the space of persistence diagrams via optimal partial transport. *arXiv preprint arXiv:1901.03048*, 2019.
- Alessio Figalli and Nicola Gigli. A new transportation distance between non-negative measures, with applications to gradients flows with dirichlet boundary conditions. *Journal de Mathématiques Pures et Appliquées*, 94(2):107–130, 2010.
- Alan V. Oppenheim and Ronald W. Schafér. *Discrete-Time Signal Processing*. Prentice Hall Press, USA, 3rd edition, 2009. ISBN 0131988425.
- Peter Lempel Søndergaard. *Finite Discrete Gabor Analysis*. PhD thesis, May 2007.
- James W Cooley and John W Tukey. An algorithm for the machine calculation of complex fourier series. *Mathematics of computation*, 19(90):297–301, 1965.
- M.J. Shensa. The discrete wavelet transform: wedding the a trous and mallat algorithms. *IEEE Transactions on Signal Processing*, 40(10):2464–2482, 1992. doi:10.1109/78.157290.
- Nan Hu, Raif Rustamov, and Leonidas Guibas. Stable and informative spectral signatures for graph matching. In *Proceedings of the IEEE Conference on Computer Vision and Pattern Recognition*, pages 2305–2312, 2014.
- Quoc Hoan Tran, Van Tuan Vo, and Yoshihiko Hasegawa. Scale-variant topological information for characterizing complex networks. *arXiv preprint arXiv:1811.03573*, 2018.
- Olympio Hacquard. Statistical learning on measures: an application to persistence diagrams. *arXiv preprint arXiv:2303.08456*, 2023.
- Zhen Zhang, Mianzhi Wang, Yijian Xiang, Yan Huang, and Arye Nehorai. Retgk: Graph kernels based on return probabilities of random walks. In *Advances in Neural Information Processing Systems*, pages 3968–3978, 2018.
- Saurabh Verma and Zhi-Li Zhang. Hunt for the unique, stable, sparse and fast feature learning on graphs. In *Advances in Neural Information Processing Systems*, pages 88–98, 2017.
- Xinyi Zhang and Lihui Chen. Capsule graph neural network. In *International Conference on Learning Representations*, 2019.

Keyulu Xu, Weihua Hu, Jure Leskovec, and Stefanie Jegelka. How powerful are graph neural networks? In *International Conference on Learning Representations (ICLR)*, 2019.

Tam Le and Makoto Yamada. Persistence fisher kernel: A riemannian manifold kernel for persistence diagrams. In *Advances in Neural Information Processing Systems*, pages 10027–10038, 2018.

Jan Reininghaus, Stefan Huber, Ulrich Bauer, and Roland Kwitt. A stable multi-scale kernel for topological machine learning. In *IEEE Conference on Computer Vision and Pattern Recognition*, 2015.

Raphael Reinauer, Matteo Caorsi, and Nicolas Berkouk. Persformer: A transformer architecture for topological machine learning, 2021.

A Proofs

This section encompasses all the mathematical proofs presented in this paper.

A.1 Proof of Proposition 4.2

We start with observing that since both measures ν and μ have the same mass and the cost of transport is $\|\mathbf{x} - \mathbf{x}'\|_1$, then $OT_1(\mu, \nu) = W_1(\mu, \nu)$. Let \mathbf{x} be a point on the shifted diagram and let \mathbf{g} be a point on the grid. Given the equivalence of the 1-optimal partial transport cost to the 1-Wasserstein metric, the cost transporting mass from \mathbf{x} to \mathbf{g} is $\|\mathbf{x} - \mathbf{g}\|_1$. The transport plan $\gamma = \Theta$ should minimize the total cost, which is the sum of the product of the transported mass and the distance it's transported. Formally, therefore we want to minimize $\sum_{i=1}^{|D|} \sum_{j=1}^{NM} \Theta_{ij} \|\mathbf{x}_i - \mathbf{g}_j\|_1$.

For each point \mathbf{x}_i in $\tau(D)$, find the closest grid point \mathbf{g}_{j^*} such that $\|\mathbf{x}_i - \mathbf{g}_{j^*}\|_1 \leq \|\mathbf{x}_i - \mathbf{g}_j\|_1$ for all $j \in \{NM\}$. We state that this assignment ensures that the transport cost for each point is as small as possible. Based on this assignment we define $\nu^* = \sum_{\mathbf{x} \in \tau(D)} m(\Theta(\mathbf{x})) \delta_{\Theta(\mathbf{x})}$.

To prove that the assignment is indeed optimal suppose by contradiction that there exist an other transport plan Θ' that reaches a lower total transport cost. There must be at least one pair $(\mathbf{x}_i, \mathbf{g}_j)$ in Θ' where \mathbf{x}_i is not transported to its closest grid point. The cost of Θ' is therefore greater than the cost of the transport plan where each \mathbf{x}_i is matched with its nearest grid point, contradicting the optimality of Θ' . \square

A.2 Proof of Theorem 4.3

We begin by stating three auxiliary lemmata, which will be proven in the upcoming sections and will be instrumental in proving Theorem 4.3.

Lemma A.1 *Let D and D' be persistence diagrams with finitely many points, and consider the mapping Θ defined in Proposition 4.2. For any bounded function f , the following inequality holds:*

$$\left\| \sum_{\mathbf{x} \in D} f(\Theta(\mathbf{x}, \omega)) - \sum_{\mathbf{x}' \in D'} f(\Theta(\mathbf{x}', \omega)) \right\|_{\infty} \leq C \left\| \sum_{\mathbf{x} \in D} f(\mathbf{x}, \omega) - \sum_{\mathbf{x}' \in D'} f(\mathbf{x}', \omega) \right\|_{\infty},$$

where C is a constant.

Lemma A.2 *Consider the Fourier transform function $f(\mathbf{x}, \omega)$ from Section 4.1. Assume that $\|\omega\|_{\infty} \leq M$.³ For all $\mathbf{x}, \mathbf{x}' \in \mathbb{R}_+^2$, we have:*

$$\|f(\mathbf{x}, \omega) - f(\mathbf{x}', \omega)\|_{\infty} \leq K \|\mathbf{x} - \mathbf{x}'\|_2,$$

where K is a finite constant value.

Lemma A.3 *Consider the Gabor transform function $f(\mathbf{t}, \mathbf{x}, \lambda, \psi, \sigma, \gamma)$ from Section 4.1. For ease of notation we will refer to it just as $f_{\lambda, \psi, \sigma, \gamma}(\mathbf{t}, \mathbf{x})$ since the other variables are just hyperparameters to tune. For all $\mathbf{x}, \mathbf{x}' \in \mathbb{R}_+^2$, we have:*

$$\|f_{\lambda, \psi, \sigma, \gamma}(\mathbf{t}, \mathbf{x}) - f_{\lambda, \psi, \sigma, \gamma}(\mathbf{t}, \mathbf{x}')\|_{\infty} \leq K' \|\mathbf{x} - \mathbf{x}'\|_2,$$

where K' is a finite constant value.

³This assumption is without loss of generality since the Fourier transform here is computed on a two-dimensional finite grid, and therefore the frequencies assume discrete finite values.

Using an argument similar to the one in Adams et al. [2017], which is aimed at proving the stability of Persistence Images, we note that, given D and D' are comprised of a finite number of points (Remark 3.2), there exists a matching γ that attains the minimum value in the Wasserstein metric.

$$\begin{aligned}
\|\Psi_\mu(f) - \Psi_\nu(f)\|_\infty &= \left\| \sum_{\mathbf{x} \in \tau(D)} f(\Theta(\mathbf{x}), \omega) - \sum_{\mathbf{x}' \in \tau(D')} f(\Theta(\mathbf{x}'), \omega) \right\|_\infty \\
&\leq C \left\| \sum_{\mathbf{x} \in \tau(D)} f(\mathbf{x}, \omega) - \sum_{\mathbf{x}' \in \tau(D')} f(\mathbf{x}', \omega) \right\|_\infty \quad \text{by Lemma A.1 on } \tau(D), \tau(D') \\
&= C \left\| \sum_{\mathbf{x} \in \tau(D)} f(\mathbf{x}, \omega) - f(\gamma(\mathbf{x}), \omega) \right\|_\infty \quad \text{since } \exists \text{ finite matching } \gamma \\
&\leq C \sum_{\mathbf{x} \in \tau(D)} \|f(\mathbf{x}, \omega) - f(\gamma(\mathbf{x}), \omega)\|_\infty \quad \text{by triangle inequality} \\
&\leq C' \sum_{\mathbf{x} \in \tau(D)} \|\mathbf{x} - \gamma(\mathbf{x})\|_2 \quad \text{by Lemma A.2 and A.3 for Fourier and Gabor transforms resp.} \\
&\leq C'' \sum_{\mathbf{x} \in D} \|\mathbf{x} - \gamma(\mathbf{x})\|_\infty \quad \text{since } \|\tau(\cdot)\|_2 \leq \sqrt{5} \|\cdot\|_\infty \text{ (see Thm 1 Adams et al. [2017])} \\
&= C'' W_1(D, D').
\end{aligned}$$

□

A.2.1 Proof of Auxiliary Lemma A.1

We start by considering the shifted diagrams $\tau(D)$ and $\tau(D')$. Applying the triangle inequality to the L^∞ norm, we can decompose the left side of the given inequality into three parts:

$$\begin{aligned}
&\left\| \sum_{\mathbf{x} \in \tau(D)} f(\Theta(\mathbf{x}, \omega)) - \sum_{\mathbf{x}' \in \tau(D')} f(\Theta(\mathbf{x}', \omega)) \right\|_\infty \\
&= \left\| \sum_{\mathbf{x} \in \tau(D)} (f(\Theta(\mathbf{x}, \omega)) - f(\mathbf{x}, \omega)) + \sum_{\mathbf{x} \in \tau(D)} f(\mathbf{x}, \omega) - \sum_{\mathbf{x}' \in \tau(D')} (f(\Theta(\mathbf{x}', \omega)) - f(\mathbf{x}', \omega)) - \sum_{\mathbf{x}' \in \tau(D')} f(\mathbf{x}', \omega) \right\|_\infty \\
&\leq \left\| \sum_{\mathbf{x} \in \tau(D)} (f(\Theta(\mathbf{x}, \omega)) - f(\mathbf{x}, \omega)) \right\|_\infty + \left\| \sum_{\mathbf{x}' \in \tau(D')} (f(\Theta(\mathbf{x}', \omega)) - f(\mathbf{x}', \omega)) \right\|_\infty + \left\| \sum_{\mathbf{x} \in \tau(D)} f(\mathbf{x}, \omega) - \sum_{\mathbf{x}' \in \tau(D')} f(\mathbf{x}', \omega) \right\|_\infty
\end{aligned}$$

Now, let $K_{max} := \sup_{\tilde{D} \in \mathcal{D}} \left\| \sum_{\mathbf{x} \in \tau(\tilde{D})} (f(\Theta(\mathbf{x}, \omega)) - f(\mathbf{x}, \omega)) \right\|_\infty$. We have that

$$\begin{aligned}
\left\| \sum_{\mathbf{x} \in \tau(D)} f(\Theta(\mathbf{x}, \omega)) - \sum_{\mathbf{x}' \in \tau(D')} f(\Theta(\mathbf{x}', \omega)) \right\|_\infty &\leq 2K_{max} + \left\| \sum_{\mathbf{x} \in \tau(D)} f(\mathbf{x}, \omega) - \sum_{\mathbf{x}' \in \tau(D')} f(\mathbf{x}', \omega) \right\|_\infty \\
&\leq \left(\frac{2K_{max}}{K_{min}} + 1 \right) \left\| \sum_{\mathbf{x} \in \tau(D)} f(\mathbf{x}, \omega) - \sum_{\mathbf{x}' \in \tau(D')} f(\mathbf{x}', \omega) \right\|_\infty,
\end{aligned}$$

where we defined $K_{min} := \inf_{\tilde{D}, \tilde{D}' \in \mathcal{D}} \left\| \sum_{\mathbf{x} \in \tau(\tilde{D})} f(\Theta(\mathbf{x}, \omega)) - \sum_{\mathbf{x}' \in \tau(\tilde{D}')} f(\Theta(\mathbf{x}', \omega)) \right\|_\infty$. Without loss of generality we assume that $K_{min} \neq 0$. By setting $C = \left(\frac{2K_{max}}{K_{min}} + 1 \right)$, we conclude the proof.

A.2.2 Proof of Lemma A.2

Using the Fourier function transform from Section 4.1 we compute:

$$\begin{aligned}
& \left\| e^{-2\pi i \mathbf{x}^\top \omega} - e^{-2\pi i \mathbf{x}'^\top \omega} \right\|_\infty \\
&= \left\| \cos(2\pi \mathbf{x}^\top \omega) - \cos(2\pi \mathbf{x}'^\top \omega) - i \left(\sin(2\pi \mathbf{x}^\top \omega) - \sin(2\pi \mathbf{x}'^\top \omega) \right) \right\|_\infty \quad \text{by Euler's formula} \\
&= \left\| -2 \sin(\pi(\mathbf{x} - \mathbf{x}')^\top \omega) \sin(\pi(\mathbf{x} + \mathbf{x}')^\top \omega) - 2i \sin(\pi(\mathbf{x} - \mathbf{x}')^\top \omega) \cos(\pi(\mathbf{x} + \mathbf{x}')^\top \omega) \right\|_\infty \quad \text{by basic trig. identities} \\
&\leq 2 \left\| \sin(\pi(\mathbf{x} - \mathbf{x}')^\top \omega) \right\|_\infty \cdot \left\| \sin(\pi(\mathbf{x} + \mathbf{x}')^\top \omega) + i \cos(\pi(\mathbf{x} + \mathbf{x}')^\top \omega) \right\|_\infty \\
&\leq 4 \left\| \sin(\pi(\mathbf{x} - \mathbf{x}')^\top \omega) \right\|_\infty \\
&\leq 4\pi \left\| (\mathbf{x} - \mathbf{x}')^\top \omega \right\|_\infty \quad \text{by } |\sin(x)| \leq |x| \\
&\leq \sqrt{2}\pi 4M \|\mathbf{x} - \mathbf{x}'\|_2 \quad \text{by Cauchy Schwarz and by } \|\omega\|_\infty \leq \sqrt{2}M \\
&\leq 8\pi M \|\mathbf{x} - \mathbf{x}'\|_\infty.
\end{aligned}$$

We can conclude the proof by taking $K = 8\pi M$.

A.2.3 Proof of Lemma A.3

We commence the proof by introducing a more concise notation. As delineated in Section 4.1, the function $f_{\lambda, \psi, \sigma, \gamma}$ is defined by the equation:

$$f_{\lambda, \psi, \sigma, \gamma}(\mathbf{t}, \mathbf{x}) = \underbrace{\exp\left(-\frac{(t_1 - x_1)^2 + \gamma^2(t_2 - x_2)^2}{2\sigma^2}\right)}_{:=\alpha_{\mathbf{x}}(\mathbf{t})} \cdot \underbrace{\exp\left(j\left(2\pi\frac{t_1 - x_1}{\lambda} + \psi\right)\right)}_{:=\beta(\mathbf{x}, \mathbf{t})}.$$

Remark A.4 *It is noteworthy that $\|\beta\|_\infty = 1$, and α is a non-negative, bounded by 1, and differentiable function. Consequently, it can be deduced that for all $\mathbf{x}, \mathbf{x}' \in \tau(D)$:*

$$\|\alpha_{\mathbf{x}} - \alpha_{\mathbf{x}'}\|_\infty \leq |\nabla\alpha| \|\mathbf{x} - \mathbf{x}'\|_2,$$

where $\nabla\alpha$ denotes the maximal directional derivative of $\alpha_{\mathbf{x}}(\mathbf{t})$. This property is derived from the fact that $|\alpha_{\mathbf{x}}(\mathbf{t}) - \alpha_{\mathbf{x}'}(\mathbf{t})| = |\alpha_{\mathbf{x}}(\mathbf{t}) - \alpha_{\mathbf{x}}(\mathbf{t} + \mathbf{x} - \mathbf{x}')| \leq |\nabla\alpha| \|\mathbf{x} - \mathbf{x}'\|_2$.

Remark A.5 *Recall that we operate under the assumption that all points in D are finite. This assumption consequently implies the existence of a finite constant L such that $\|\nabla\alpha\|_\infty \leq L$.*

We now compute:

$$\begin{aligned}
\|f_{\lambda, \psi, \sigma, \gamma}(\mathbf{t}, \mathbf{x}) - f_{\lambda, \psi, \sigma, \gamma}(\mathbf{t}, \mathbf{x}')\|_\infty &= \|\alpha_{\mathbf{x}}(\mathbf{t}) \cdot \beta(\mathbf{x}, \mathbf{t}) - \alpha_{\mathbf{x}'}(\mathbf{t}) \cdot \beta(\mathbf{x}', \mathbf{t})\|_\infty \\
&= \|\alpha_{\mathbf{x}}(\mathbf{t}) \cdot \beta(\mathbf{x}, \mathbf{t}) - \alpha_{\mathbf{x}}(\mathbf{t}) \cdot \beta(\mathbf{x}', \mathbf{t}) + \alpha_{\mathbf{x}}(\mathbf{t}) \cdot \beta(\mathbf{x}', \mathbf{t}) - \alpha_{\mathbf{x}'}(\mathbf{t}) \cdot \beta(\mathbf{x}', \mathbf{t})\|_\infty \\
&\leq \|\beta\|_\infty \|\alpha_{\mathbf{x}}(\mathbf{t}) - \alpha_{\mathbf{x}'}(\mathbf{t})\|_\infty + \|\alpha\|_\infty \|\beta(\mathbf{x}, \mathbf{t}) - \beta(\mathbf{x}', \mathbf{t})\|_\infty \\
&\leq |\nabla\alpha| \|\mathbf{x} - \mathbf{x}'\|_2 + 2 \quad \text{from Remark A.4} \\
&\leq L \|\mathbf{x} - \mathbf{x}'\|_2 + 2 \quad \text{from Remark A.5} \\
&\leq K \|\mathbf{x} - \mathbf{x}'\|_2 \quad \text{for some constant } K.
\end{aligned}$$

B Complementary material

This section includes extensive tables that provide a comparative analysis of graph data and dynamical particles classification scores for various methods studied in this paper.

Dataset/Grid	FOURIER		Real V. GABOR		WT-db1		WT-db2		WT-db3		WT-coif1		WT-coif2		WT-coif3		
	Mean	Max	Mean	Max	Mean	Max	Mean	Max	Mean	Max	Mean	Max	Mean	Max	Mean	Max	
MUTAG	20	87.8(±.8)	88.9	88.2(±.9)	89.4	87.8(±.8)	88.9	87.8(±.8)	88.9	88.7(±1.0)	90.6	88.6(±.8)	90.0	87.7(±1.2)	90.0	87.5(±.9)	89.4
	32	89.1(±1.2)	91.1	89.7(±1.0)	91.1	88.4(±1.3)	90.0	88.6(±1.0)	90.0	88.9(±1.0)	90.6	88.9(±.7)	90.0	89.7(±.5)	90.6	89.8(±.9)	91.7
	50	88.1(±1.1)	89.4	87.8(±1.2)	89.4	86.9(±1.1)	88.9	87.6(±.9)	88.9	88.3(±1.4)	91.1	88.2(±.9)	89.4	88.3(±1.1)	90.0	88.1(±.6)	88.9
DHFR	20	77.8(±.7)	78.9	76.8(±.8)	78.3	77.8(±.6)	78.9	78.3(±.7)	78.9	79.3(±.6)	80.0	78.5(±.6)	79.6	79.2(±1.0)	81.2	79.0(±.8)	80.4
	32	79.1(±1.0)	80.5	78.3(±.7)	79.5	81.5(±.7)	83.1	81.8(±.7)	82.9	81.1(±1.0)	82.4	81.4(±.5)	82.1	80.7(±.5)	82.4	80.6(±.7)	81.9
	50	79.6(±.7)	81.2	78.5(±.8)	80.0	80.6(±.4)	81.2	80.2(±.4)	80.8	80.7(±.4)	81.5	81.0(±.5)	81.9	81.5(±.5)	82.3	80.9(±.9)	82.7
COX2	20	78.3(±.6)	78.9	80.6(±1.0)	82.4	79.2(±.7)	80.4	79.7(±.7)	81.1	79.7(±.7)	80.9	80.0(±.4)	80.4	79.7(±.5)	80.4	79.5(±.8)	81.5
	32	76.7(±.7)	77.8	78.4(±.8)	80.0	77.3(±1.0)	79.3	78.0(±1.0)	79.3	78.0(±1.1)	79.3	78.0(±.6)	78.9	78.2(±.6)	78.9	77.4(±.8)	78.5
	50	77.1(±.9)	78.3	79.5(±.8)	81.3	77.5(±.7)	78.5	78.2(±.5)	78.9	77.7(±.6)	78.9	78.7(±.7)	80.0	78.2(±1.0)	79.3	78.8(±1.2)	80.2
PROTEINS	20	72.5(±.6)	73.2	72.7(±.3)	73.1	72.4(±.4)	72.8	72.5(±.7)	73.4	72.6(±.6)	73.4	72.8(±.6)	73.6	72.3(±.5)	73.0	72.1(±.4)	72.9
	32	71.9(±.5)	72.8	72.3(±.5)	73.1	72.1(±.5)	72.9	72.3(±.5)	73.1	72.3(±.5)	73.3	72.3(±.6)	73.4	71.9(±.5)	73.0	72.1(±.8)	73.0
	50	71.9(±.6)	72.7	72.3(±.6)	73.4	72.1(±.5)	73.1	72.4(±.6)	73.2	72.4(±.6)	73.2	72.7(±.5)	73.5	72.6(±.5)	73.5	72.6(±.5)	73.3
IMDB-B	20	67.6(±.6)	68.6	67.7(±.5)	68.6	67.5(±.8)	68.7	67.1(±.6)	68.3	67.0(±.6)	67.7	67.1(±.3)	67.5	66.8(±.7)	67.9	66.4(±.9)	68.3
	32	66.7(±.5)	67.7	67.4(±.7)	68.6	66.4(±.9)	68.3	66.9(±.8)	67.9	67.2(±.6)	67.9	66.7(±.8)	67.7	66.8(±.6)	67.7	66.8(±.6)	67.8
	50	67.5(±.8)	69.1	68.4(±.7)	69.8	68.2(±.6)	69.3	68.1(±.7)	69.2	67.4(±.8)	68.5	68.2(±.7)	69.1	67.7(±.4)	68.3	67.7(±.5)	68.5
IMDB-M	20	42.2(±.5)	43.1	42.0(±.4)	42.7	42.4(±.4)	42.9	42.2(±.5)	42.9	42.5(±.3)	43.3	42.3(±.7)	43.5	42.3(±.3)	42.8	42.5(±.4)	43.2
	32	42.8(±.5)	43.7	42.5(±.4)	43.2	42.8(±.5)	43.9	42.5(±.4)	43.5	43.1(±.5)	43.9	42.9(±.5)	43.6	42.7(±.4)	43.5	42.6(±.5)	43.8
	50	42.9(±.5)	43.7	42.9(±.2)	43.3	43.0(±.5)	43.6	43.3(±.6)	44.4	43.1(±.5)	43.9	42.9(±.3)	43.5	43.7(±.5)	43.9	43.3(±.4)	44.1

Table 3: Comparative analysis of graph data classification scores of the methods presented in this study.

Dataset/Grid	FOURIER	Real V. GABOR	WT-db1	WT-db2	WT-db3	WT-coif1	WT-coif2	WT-coif3
Orbit5K	64	81.0(±1.1)	82.2(±.8)	82.8(±.9)	80.8(±.7)	81.1(±.9)	81.0(±.9)	81.3(±.6)
	128	83.4(±1.0)	82.7(±.7)	82.2(±.7)	83.4(±.6)	83.8(±.7)	83.6(±1.1)	84.6(±.8)

Table 4: Comparative analysis of Orbit5K classification scores of the methods presented in this study.